nature photonics

ARTICLES

https://doi.org/10.1038/s41566-019-0464-9

Efficient telecom-to-visible spectral translation through ultralow power nonlinear nanophotonics

Xiyuan Lu[1,2*], Gregory Moille[1,2], Qing Li[1,2,3], Daron A. Westly[1], Anshuman Singh[1,2], Ashutosh Rao[1,2], Su-Peng Yu[4,5], Travis C. Briles[4,5], Scott B. Papp[4,5] and Kartik Srinivasan[1,6*]

The ability to spectrally translate lightwave signals in a compact, low-power platform is at the heart of the promise of nonlinear nanophotonic technologies. For example, a device to connect the telecommunications band with visible and short near-infrared wavelengths can enable a connection between high-performance chip-integrated lasers based on scalable nanofabrication technology with atomic systems used for time and frequency metrology. Although second-order nonlinear ($\chi^{(2)}$) systems are the natural approach for bridging such large spectral gaps, here we show that third-order nonlinear ($\chi^{(3)}$) systems, despite their typically much weaker nonlinear response, can realize spectral translation with unprecedented performance. By combining resonant enhancement with nanophotonic mode engineering in a silicon nitride microring resonator, we demonstrate efficient spectral translation of a continuous-wave signal from the telecom band (~1,550 nm) to the visible band (~650 nm) through cavity-enhanced four-wave mixing. We achieve such translation over a wide spectral range >250 THz with a translation efficiency of (30.1 ± 2.8)% and using an ultralow pump power of (329 ± 13) μW. The translation efficiency projects to (274 ± 28)% at 1 mW and is more than an order of magnitude larger than what has been achieved in current nanophotonic devices.

At its heart, nonlinear optics[1,2] enables the creation of spectral tones at frequencies that are different than those at the input of the optical system. As the name implies, such functionality is typically unavailable at low optical powers in solid-state systems, where most materials tend to exhibit only a linear optical response. In addition, the spectral separation between the generated and input frequencies is often limited by the dispersive properties of common nonlinear media, which make phase-matching challenging. Nanophotonic systems, however, can realize large optical intensities for modest input powers due to the strong field confinement and long photon lifetimes provided in resonator geometries. The strong field confinement also creates geometric dispersion to balance material dispersion, so that phase matching can be achieved for wide frequency separations. Here, we demonstrate a chip-scale system that links telecommunications-band photons and visible-wavelength photons over a spectral separation of >250 THz, via ultralow-power nonlinear nanophotonics, with a high translation efficiency achieved for sub-milliwatt pump power. The performance of our platform, quantified by translation efficiency relative to pump power, exceeds that of chip-integrated second-order nonlinear ($\chi^{(2)}$) systems, despite our use of the much weaker third-order nonlinear ($\chi^{(3)}$) effect. Our work illustrates the ability to use resonant enhancement and precise nanophotonic device engineering to dramatically enhance nonlinear optical processes.

Such spectral translation, that is, the ability to bridge widely separated optical frequencies, has many applications. For example, high-performance tunable lasers have been developed in the context of heterogeneously integrated silicon photonics[3,4], but their operating wavelengths are restricted to >1,100 nm due to the materials involved. Spectral translation to shorter wavelengths, for example, the short near-infrared and visible, can make such sources suitable for spectroscopy of atomic systems, for applications such as wavelength references and optical clocks[5]. Moreover, the potential to link visible-wavelength systems together with telecom signals can be important in the context of long-distance fibre-optic distribution of timing and sychronization signals[6].

Nanophotonic spectral translation

Various forms of spectral translation have been realized using $\chi^{(2)}$ or $\chi^{(3)}$ in several different platforms, including $LiNbO_3$ (refs. [7–10]), Si (ref. [11]), Si_3N_4 (refs. [12–16]), SiO_2 (refs. [17,18]), AlN (refs. [19–21]), GaAs (refs. [22–24]), GaP (ref. [25]) and AlGaAs (ref. [26]). The $\chi^{(2)}$ nonlinear optical process has been the major workhorse for spectral translation across widely separated wavelengths for two main reasons. First, the magnitude of the nonlinear response resulting from the $\chi^{(2)}$ coefficient is much larger than that of higher-order nonlinearities. For example, in bulk nonlinear crystals, the laser intensity needs to be comparable to the strength of a characteristic atomic field ($I_{at} = 3.5 \times 10^{20}\,W\,m^{-2}$) for the nonlinear response of a $\chi^{(3)}$ process to match that of a $\chi^{(2)}$ process[1]. Second, $\chi^{(2)}$ processes such as second-harmonic generation (SHG) and sum-frequency generation (SFG) naturally result in large spectral separations. On the other hand, $\chi^{(3)}$ nonlinear optics, within Si_3N_4 devices in particular, though having seen successful use in quantum frequency conversion[13], entangled photon-pair generation[27], octave-span frequency comb generation[28–30] and optical frequency synthesis[4], generally does not meet the performance levels of state-of-the-art $\chi^{(2)}$ spectral translation[8] in terms of the combination of efficiency, range and required pump power. For example, millimetre-scale $LiNbO_3$ resonators reach 9% conversion efficiency at 30 μW pump power[8], while in $\chi^{(3)}$ platforms, such a conversion efficiency has only been realized for wide spectral separations at much higher (tens of milliwatts) pump power[11,13].

[1]Microsystems and Nanotechnology Division, Physical Measurement Laboratory, National Institute of Standards and Technology, Gaithersburg, MD, USA. [2]Maryland NanoCenter, University of Maryland, College Park, MD, USA. [3]Electrical and Computer Engineering, Carnegie Mellon University, Pittsburgh, PA, USA. [4]Time and Frequency Division, Physical Measurement Laboratory, National Institute of Standards and Technology, Boulder, CO, USA. [5]Department of Physics, University of Colorado, Boulder, CO, USA. [6]Joint Quantum Institute, NIST/University of Maryland, College Park, MD, USA. *e-mail: xiyuan.lu@nist.gov; kartik.srinivasan@nist.gov

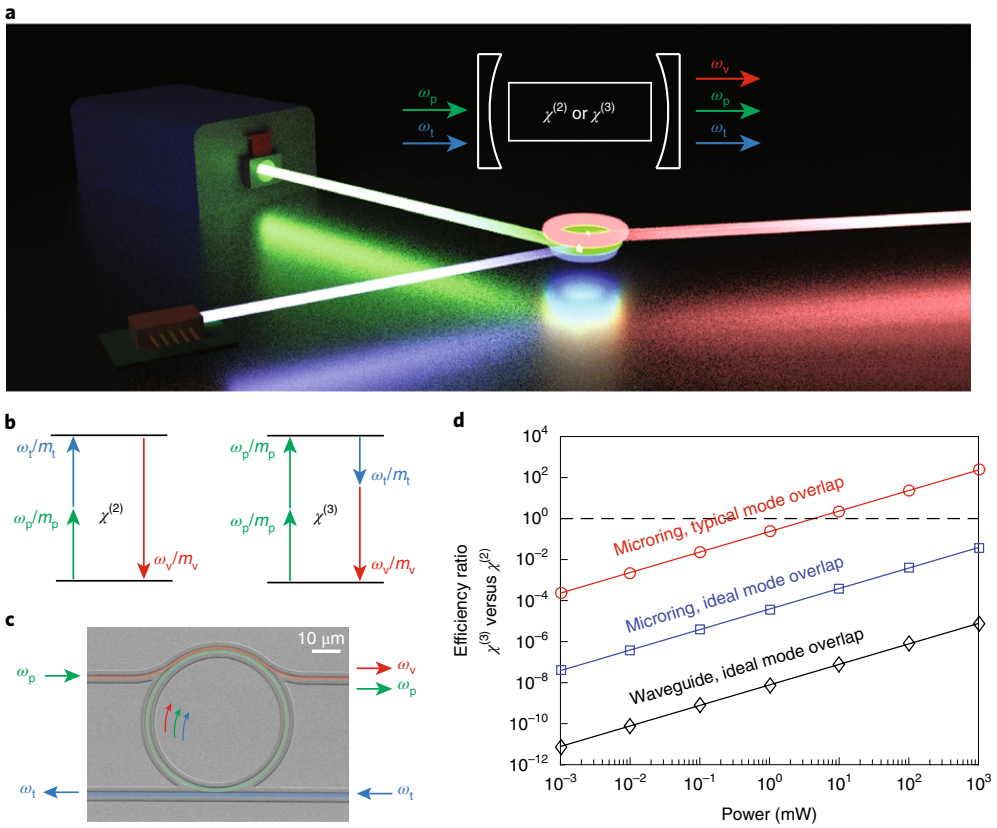

Fig. 1 | Nanophotonic telecom-to-visible spectral translation and efficiency comparison. a, Nanophotonic spectral translation uses a cavity-enhanced second-order or third-order nonlinear optical process ($\chi^{(2)}$ or $\chi^{(3)}$) to efficiently transfer light into a new frequency with ultralow laser pump power (see inset for a simplified scheme). ω_p, ω_t and ω_v represent frequencies for pump, telecom and visible light, respectively. **b**, Energy and momentum conservation requirements for SFG (left) and dFWM (right) processes with single fundamental mode family (SFMF) operation. **c**, False-coloured scanning electron microscope image of the nanophotonic device and the coupling scheme we use for spectral translation. The top pulley waveguide (red) and the bottom straight waveguide (blue) are used to couple pump/visible and telecom light, respectively, into and out of the microring (green). **d**, Order-of-magnitude comparison of the translation efficiency for the two processes in **b** with the device geometry of **c**. For a microring with a finesse of $\mathcal{F} \approx 5{,}000$ (red), the efficiency of the $\chi^{(3)}$ process can compete with, or even exceed, that of the $\chi^{(2)}$ process at milliwatt pumping levels, if the mode overlap can be sufficiently well-optimized. See Supplementary Information for details.

Nanophotonic spectral translation uses optical resonators to enhance the nonlinear optical processes (Fig. 1a), which enables ultralow pump power operation at the expense of bandwidth, so that the primary application is translation of continuous-wave (c.w.) signals. We propose that, for telecom-to-visible spectral translation, high-Q resonators with proper nanophotonic mode engineering can enable $\chi^{(3)}$ spectral translation to be comparable to the current state-of-the-art $\chi^{(2)}$ process. To illustrate this point, we compare the translation efficiency of $\chi^{(2)}$ and $\chi^{(3)}$ processes, for example, SFG and degenerate four-wave mixing (dFWM) (Fig. 1b), in microring/waveguide geometries (Fig. 1c) using parameters for Si_3N_4 and $LiNbO_3$ as representative of $\chi^{(3)}$ and $\chi^{(2)}$ media, respectively (Fig. 1d). Translation efficiency is defined as the ratio of on-chip power between the visible translated signal and input telecom signal (see Methods for details). As described in the Supplementary Information, the ratio of the efficiency of the $\chi^{(3)}$ process to that of the $\chi^{(2)}$ process scales with pump power, so that a sufficiently large pump power can make these two processes comparable in efficiency. In the waveguide, the $\chi^{(3)}$ process is much weaker than $\chi^{(2)}$ for all powers considered, with a ratio of approximately −81 dB at 1 mW pump power (black). In a high-finesse microring ($\mathcal{F} \approx 5{,}000$) due to the cavity enhancement of the field intensity, the difference between these two processes becomes smaller, approximately−44 dB at 1 mW (blue). Mode matching is assumed to be ideal in the above estimates. However, in practice, demonstrated $\chi^{(2)}$ nonlinear resonators have typically exhibited non-ideal mode overlap[7,8], particularly in larger resonators that support many mode families so that mode identification is challenging. In contrast, accurate mode identification has been demonstrated recently in Si_3N_4 nanophotonics[27], providing an opportunity for cavity-enhanced $\chi^{(3)}$ to exhibit an efficiency comparable to $\chi^{(2)}$ if an optimized mode overlap is realized. For example, the red curve in Fig. 1d indicates that an optimized $\chi^{(3)}$ process can be as efficient as current state-of-the-art $\chi^{(2)}$ at milliwatt-level pump powers.

To achieve such an optimized $\chi^{(3)}$ spectral translation, three core elements are required for the the nonlinear optical resonator (Fig. 1c) and its mode engineering. First, simultaneous frequency matching and phase matching are required to satisfy energy conservation and momentum conservation (Fig. 1b). Second, a high quality factor (Q) and strong modal confinement are required to create large circulating optical intensities. Third, large spatial overlap between the modes is critical to maximize the interaction efficiency. We use cavity-enhanced dFWM in a Si_3N_4 microring resonator (Fig. 1c) to translate a c.w. signal at 1,573 nm to a visible wavelength at 670 nm (a spectral range over 250 THz), with a translation efficiency of $(30.1 \pm 2.8)\%$ at only $(329 \pm 13)\,\mu W$ pump power. This value projects to $(274 \pm 28)\%$ at 1 mW, at least one order of magnitude higher

than that reported from other nanophotonic devices, and is comparable to the best result using a $\chi^{(2)}$ process, achieved using millimetre-scale resonators[8].

System design

The previous theoretical analysis shows that both optical quality factor and nanophotonic mode engineering play critical roles for the efficiency of the $\chi^{(3)}$ spectral translation. Our design target here is therefore a mode overlap of approximately 100% for the dFWM process and a large Q/V for all three interacting modes (in the telecom, pump and visible bands). As a practical matter, we prefer geometries that support a limited number of mode families (particularly in the visible), to ease the task of identifying and employing the targeted optical modes. Moreover, efficiently coupling the telecom, pump and visible modes of the microring to the access waveguide is also necessary, both for coupling the pump/signal light into the microring and extracting the translated light out of the microring. We outline the basic design principles in this section, and present more details in Supplementary Section II.

The dispersion engineering required for a microring differs from that for a straight waveguide, in which phase matching means that linear momentum of the input/output photons must be conserved. In a microring, phase matching applies to the momentum of the whispering gallery modes along the azimuthal direction. We define the whispering gallery modes with the same polarization and radial mode order to be within one mode family. Within each mode family, a whispering gallery mode is specified by its azimuthal number m (electric field varies along the azimuthal angle ϕ as $e^{im\phi}$). The phase-matching condition for modes of the same family becomes a mode number-matching criterion, that is, $\Delta m = 0$. For dFWM, the criterion is $2m_p - m_t - m_v = 0$, where $m_p/m_t/m_v$ are the azimuthal mode numbers for the pump/telecom (input signal)/visible (translated signal) modes[31].

Once $\Delta m = 0$ is satisfied for an appropriate set of modes, the energy conservation condition requires $2\omega_p - \omega_t - \omega_v = 0$, and the involved pump/telecom/visible fields ($\omega_p/\omega_t/\omega_v$) all have to be in resonance with their corresponding cavity modes ($\hat{\omega}_p/\hat{\omega}_t/\hat{\omega}_v$), which can be challenging for high-Q cavities due to their narrow spectral widths. The maximum allowable frequency mismatch for the dFWM process is dictated by the loaded Q of the corresponding cavity modes, that is, $\delta\omega_{p,t,v} = |\omega_{p,t,v} - \hat{\omega}_{p,t,v}| < \hat{\omega}_{p,t,v}/2Q_{p,t,v}$. This stringent frequency-matching requirement represents a major challenge for nanophotonic devices, necessitating the matching of frequencies separated over hundreds of terahertz with an accuracy within a cavity linewidth, for example, ~1 GHz for a loaded Q of 2×10^5 at a telecom wavelength.

Achieving such mode number and frequency matching is a non-trivial task, in particular considering the >250 THz spectral separation. Our approach differs somewhat from other microcavity nonlinear optics works. For intraband FWM, mode number matching can be achieved simply by counting the number of free spectral ranges (FSRs) between the modes and therefore absolute mode numbers are not needed, as only mode number differences are used. To ensure that the corresponding mode frequencies line up appropriately, resonator dispersion parameters are often used to design an appropriate geometry, as the approximation of the modal spectrum (that is, the position of the resonance frequencies as a function of azimuthal mode number) by a truncated polynomial fit is appropriate. However, for wideband spectral translation, we find that it is more accurate to design devices by directly working with the resonance frequencies as determined by fully vectorial finite-element simulations, which is equivalent to saying that we include all orders of dispersion in the calculation (we ignore Kerr frequency shifts due to the low pump powers employed in our experiments). We then use the accurate and unambiguous mode number identification technique from ref. [27] to experimentally identify the targeted cavity modes, determine their frequency mismatch and, if sufficiently small, conduct FWM experiments.

Our microring geometry uses a stochiometric Si_3N_4 core, bottom SiO_2 cladding and top air cladding. This has two main benefits. First, it allows post-processing for fine tuning of the cavity mode frequencies. Post-fabrication reactive-ion etching is used to reduce device height while maintaining the device lateral dimensions. Hot phosphoric acid etching changes the device height and lateral dimensions simultaneously with nanometre accuracy. These two post-processing methods, when used with ellipsometric measurements, enable fine tuning of the targeted mode sets (for more details see Supplementary Section II and Supplementary Table 1). Second, as described below, the asymmetric cladding allows for separation of the coupling tasks for pump/visible and telecom modes in a manner that would be difficult to implement in symmetrically oxide-clad devices, by taking advantage of waveguide cutoff[32].

Single fundamental mode family engineering

Going beyond phase and frequency matching, the heart of our design is single fundamental mode family (SFMF) engineering, where all three interacting modes are in the fundamental transverse-electric mode family (TE1), with the dominant electric field component in the radial direction (insets, Fig. 2c). The benefits of SFMF engineering are twofold. First, fundamental modes typically have the highest Q values, maximizing the resulting optical intensities (for a given pump power) that are critical for the efficiency of the spectral translation process. Second, SFMF engineering can achieve a mode overlap of approximately 90% for dFWM across telecom, pump and visible bands (see Supplementary Fig. 2 for details). We note that, although the use of fundamental modes for nonlinear processes is common within the telecommunications band, for example, in spontaneous FWM devices[33], for operation over widely separated frequencies, higher-order modes are often used. For example, $\chi^{(2)}$ nanophotonic devices used in SHG generally involve a higher-order mode family for the SHG mode. In addition to lower Q factors, their overlap with fundamental modes is far from ideal—it is negligible between TE1 and TE2, and approximately 30% for TE1 and TE3 in our geometry.

To demonstrate the potential range of $\chi^{(3)}$ spectral translation, we targeted a spectral translation window that is over one octave (that is, comparable to SFG), in translating a telecom wavelength of 1,570 nm to a wavelength of 670 nm by a pump located at 940 nm. A schematic of the nanophotonic spectral translation device is presented in Fig. 2a. The microring is defined by three parameters, its height (H), outer ring radius (RR) and ring width (RW). These parameters yield geometric dispersion (combination of waveguiding and bending effects) that compensates material dispersion and enables simultaneous phase and frequency matching. We chose $H = 500$ nm, RR = 25 μm and RW = 1,150 nm to target the selected dFWM wavelengths. More details regarding geometry determination and parameter sensitivity are provided in Supplementary Section II-A. A finite-element-method simulation is carried out to determine the frequency- and phase-matched mode sets for the TE1 family (Fig. 2b) for this geometry. For a pump wavelength of approximately 940 nm, we have frequency- and phase-matched telecom and visible modes near 1,570 nm and 670 nm, respectively. The frequency matching criterion used in this simulation is $\Delta\omega/(2\pi) < 1$ GHz.

The wide spectral separation of the dFWM process requires careful waveguide–microring coupling design. We used two waveguides to separate the coupling tasks, as shown in Fig. 2a. The top pulley waveguide[13] is wrapped around the microring to provide a 33 μm interaction length that couples the 940 nm and 670 nm modes efficiently. This waveguide has a width of 560 nm and supports single-mode operation at 940 nm, while being cut off (that is, does not support any mode) at 1,550 nm. The bottom straight

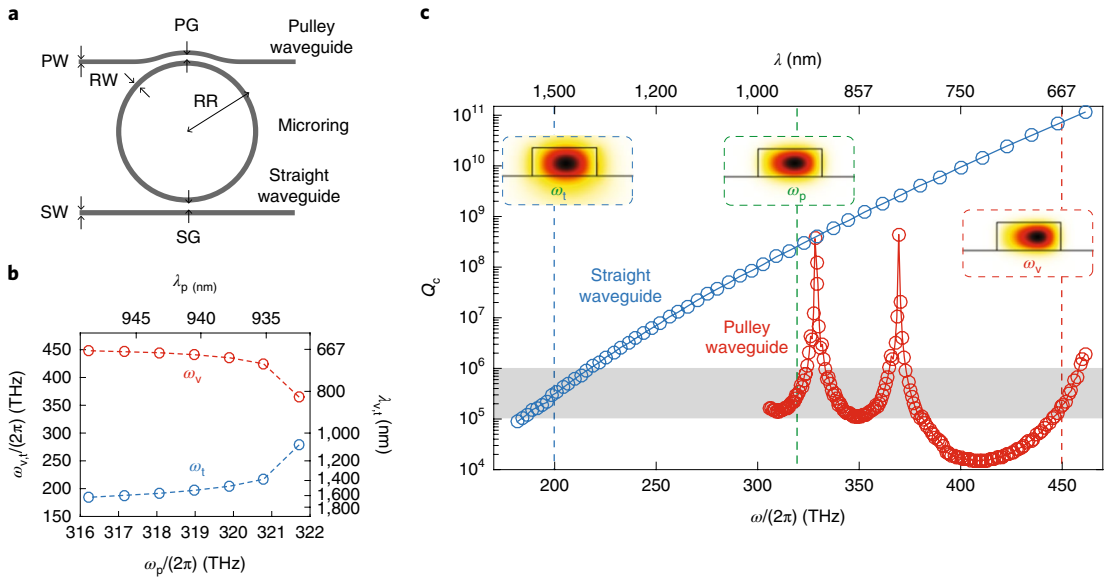

Fig. 2 | Design for telecom-to-visible spectral translation. a, Device scheme. RR/RW, ring outer radius/ring width; PW/PG, pulley waveguide width/gap; SW/SG, straight waveguide width/gap. **b**, Simulations of the frequency/phase-matched wavelengths. The *m* numbers for each set of three modes (that is, each set of frequencies) satisfy $(2m_p = m_t + m_v)$, with a frequency mismatch $\Delta\omega/(2\pi) = |2\omega_p - \omega_t - \omega_v|/(2\pi)$ within 1 GHz. Simulation parameters are $H = 500$ nm, RR = 25 μm and RW = 1,158 nm. **c**, Wavelength-dependent coupling of the pulley (red) and straight (blue) waveguides. Targeted values are typically $Q_c = 1\times10^5$ to 1×10^6 (grey area). All modes are fundamental transverse electric modes (TE1). Insets: cross-sectional views of the dominant electric field amplitude (in the radial direction of the microring). Simulation parameters (in addition to **b**): PW = 560 nm, PG = 170 nm, SW = 1,120 nm and SG = 425 nm.

waveguide has a width of 1,120 nm and is single mode at 1,550 nm. The wavelength-dependent coupling Q factors (Q_c) were calculated using coupled mode theory[13,34], and are shown in Fig. 2c for both straight waveguide (blue) and pulley waveguide (red). The targeted Q_c is 1×10^5 to 1×10^6, which is indicated by the grey area. The straight waveguide couples the 1,570 nm mode efficiently, but essentially does not couple the 940 nm and 670 nm modes at all (severe undercoupling due to the large coupling gap). The pulley waveguide, while cut off at telecom wavelengths, couples the 940 nm and 670 nm modes efficiently.

Device characterization

The device design described in the previous section was fabricated (see Methods) and characterized experimentally (see Supplementary Fig. 3 for the experimental set-up). The cavity linear transmission spectrum is shown in Fig. 3a, where the traces indicated by different colours were measured using separate lasers. For TE polarization, the transmission spectrum shows a single-mode family in the telecom band and only two mode families that are relatively efficiently coupled in the pump and visible bands. The TE1 coupling is indeed reasonably efficient as designed, with 670 nm, 940 nm and 1,550 nm modes overcoupled, nearly critically coupled and slightly undercoupled, respectively. The intrinsic Q values are $(1.13\pm0.01)\times10^6$, $(8.32\pm0.19)\times10^5$ and $(5.29\pm0.14)\times10^5$, respectively, for the visible, pump and telecom modes. The loaded Q factors are $(2.77\pm0.02)\times10^5$, $(3.04\pm0.07)\times10^5$ and $(1.17\pm0.03)\times10^5$, respectively, with the transmission traces and fits shown in Fig. 3b. The uncertainties are one standard deviation values resulting from the Lorentzian fits. The candidate set of mode numbers for dFWM is 442, 301 and 160, and is identified using a mode splitting method that targets nearby azimuthal modes[27,35].

As an approach to evaluate whether the chosen set of phase-matched modes is indeed frequency-matched, we use spontaneous photon pair generation. When phase matching and frequency matching are satisfied, both spontaneous and stimulated degenerate FWM can occur. We can thus use the spontaneous photon-pair spectra to evaluate the phase and frequency matching for the stimulated process in the regime for which nonlinear frequency shifts are small[36]. We record the spontaneous photon-pair spectra with a 939.5 nm pump and without any narrow-band filters in Fig. 3c,d. The brightest set of spectral tones are at 669.8 nm/1,572.7 nm, and the adjacent modes are >16 dB smaller (inset, Fig. 3c). The photon-pair spectrum suggests that good phase and frequency matching has been achieved for the aforementioned mode set.

Spectral translation

Spectral translation is then initiated by sending to the device an input telecom signal at 1,572.7 nm in addition to the pump laser at 939.5 nm. The measured optical spectra from the pulley and straight waveguide outputs are overlaid in Fig. 4a. These spectra are taken directly from the waveguides using lensed single-mode optical fibres without any filters, and confirm that the stimulated process translates the 1,572.7 nm signal to 669.8 nm. We observe that the pulley waveguide (red) outcouples pump and visible light, while the straight waveguide (blue) outcouples telecom light. The isolation at 1,572.7 nm in the pulley waveguide is approximately 40 dB, consistent with the waveguide cutoff previously described, while the straight waveguide, as expected, does not show appreciable outcoupling of the visible translated signal. The spectra are relatively clean, with no broadband or narrowband noise or competing FWM tones observed (the small peak near 1,340 nm is an artefact of the optical spectrum analyser).

To optimize the translation efficiency at a certain pump power, both pump and telecom lasers need to be tuned into their respective resonances. Because the dispersion of the modes is close to ideal, as indicated by Fig. 3c,d, and the nonlinear frequency shift is small at this sub-milliwatt pump power level, the optimization of the visible signal is simply optimizing the pump and telecom powers dropped into the ring, that is, tuning the laser close to the centre of the transmission dip of the resonances. This process is shown in Fig. 4c–e. When the pump laser is tuned into the cavity, as indicated by the circles in the thermal bistability trace (Fig. 4c), the telecom mode also

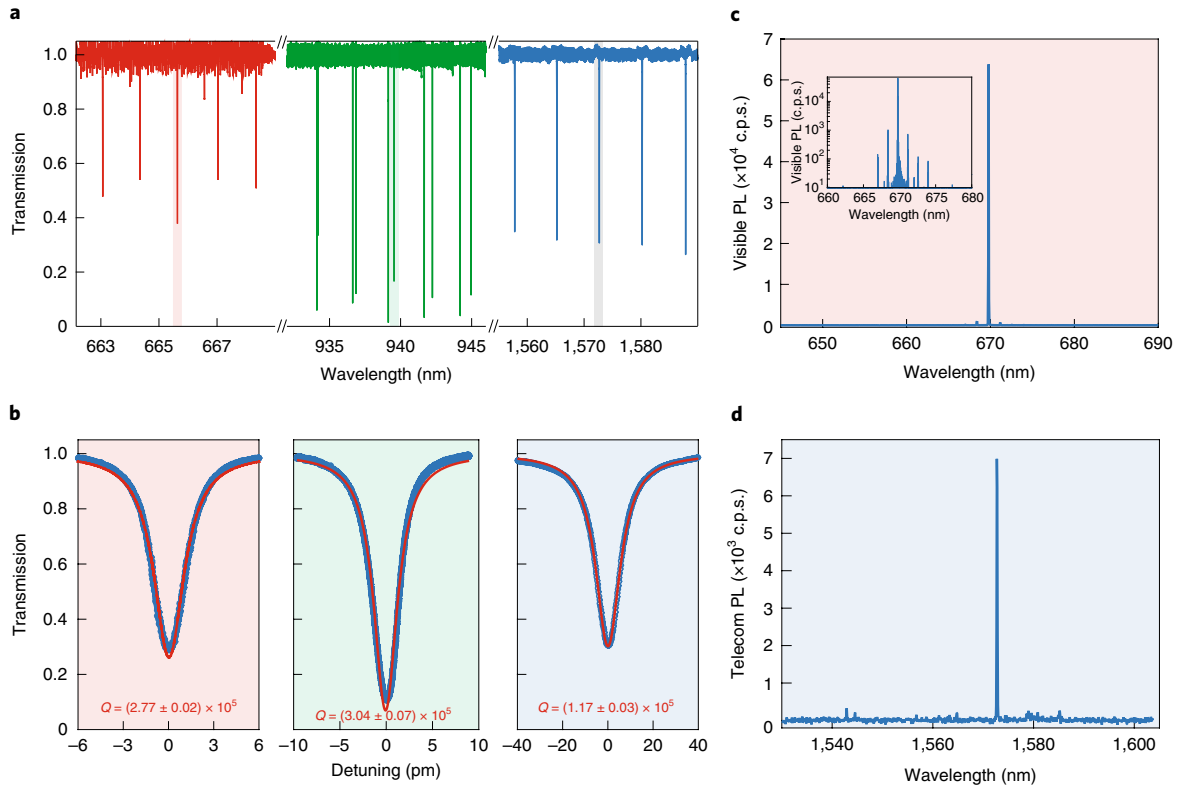

Fig. 3 | Assessment of device *Q*, coupling, and phase and frequency matching. a, Cavity transmission for the spectral translation device in the visible, pump and telecom bands, with device parameters as prescribed in Fig. 2c. **b**, Enlarged view of transmission traces for TE1 modes at 665.8 nm (red), 939.5 nm (green) and 1,572.7 nm (blue) from left to right with loaded *Q* factors of approximately 1×10^5 to 3×10^5 estimated by Lorentzian fitting (red lines). **c**,**d**, Photon pair spectrum generated by spontaneous FWM in the visible band (**c**) and the telecom band (**d**), with a degenerate pump at 939.5 nm. The inset to **c** shows the visible spectrum in log scale. The 669.8 nm/1,572.7 nm photon-pair spectra are free from broadband noise and are >16 dB larger than adjacent mode sets, which indicates good frequency and phase matching for the dFWM process.

experiences thermal bistability due to the pump intracavity heating, and therefore the telecom laser needs to be detuned to follow this thermal shift by searching for the minimal telecom transmission (Fig. 4d). The translation efficiency is optimized when the pump laser is close to zero detuning, as shown in Fig. 4e.

We optimize the translation efficiency at various pump/signal power levels and show the power dependence in Fig. 4f,g. To measure the translated power accurately, we use a dichroic filter to separate the 939.5 nm pump and 669.8 nm translated signal (Fig. 4b; see Supplementary Information for details). The pump power dependence of the telecom-to-visible translation efficiency is plotted in Fig. 4f, where the observed quadratic behaviour (red lines) is a signature of the degenerate pump in the dFWM process. Two types of efficiency, that is, translation efficiency (η) and quantum efficiency (η_Q), are plotted. As defined earlier, the translation efficiency is based on a ratio of powers and is consistent with what is often quoted in classical applications (such as SHG), while quantum efficiency is defined in terms of photon flux (see Methods for the precise definitions). A peak translation efficiency $\eta=(30.1\pm2.8)\%$ is reached, corresponding to a quantum efficiency of $\eta_Q=(12.8\pm1.2)\%$. At the highest measured pump power of $(414\pm17)\,\mu W$, the translation efficiency drops due to close-to-pump parametric oscillation and cascaded FWM and its consumption of pump power. The consumption of pump power can be partly verified by the reduction in resonance contrast in the pump transmission traces (inset, Fig. 4f). This issue can potentially be addressed in the future by advanced dispersion or coupling designs to suppress the competing process.

The translated signal power at 669.8 nm has a linear dependence on the input power at 1,572.7 nm, as shown in Fig. 4g for an intermediate pump power of $(165\pm7)\,\mu W$. The linear fit (red line) yields a translation efficiency $\eta=(7.5\pm0.4)\%$. The efficiency is taken with pump detuning kept at a constant level indicated by the inset of Fig. 4g. The maximum signal power here is $(533\pm11)\,\mu W$, which is larger than the pump power of $(165\pm7)\,\mu W$, while the translation efficiency is still not saturated. This is possible because the pump photon number/energy in the microring is sufficient, as a result of higher optical quality factor and better waveguide–microring coupling for the 940 nm mode. An even higher telecom power leads to pump depletion and loss of the fixed pump detuning due to the thermal bistability of the cavity mode. For applications that need higher powers, the pump power can be increased as shown in Fig. 4f, up to the point where competing FWM processes ultimately limit the pump power available for spectral translation (see Supplementary Section IV for details). That being said, the spectrally translated visible powers we demonstrate (in the tens of microwatts range in Fig. 4g) are already suitable for applications in atomic spectroscopy and laser stabilization. In the future, one could envision combining the Si_3N_4 nonlinear nanophotonics we demonstrate with recent advances in building miniaturized atomic vapour cells addressed by integrated photonic circuits (for example, ref. [37]).

Comparison

To evaluate the performance of our nanophotonic device among state-of-the-art wide-band spectral translation devices, we compare it with reported results from the literature in Table 1. In this table we consider material platform, device geometry, nonlinear process, dimensions, operation wavelengths, pump power, demonstrated efficiency and expected efficiency at 1 mW pump power. Our device

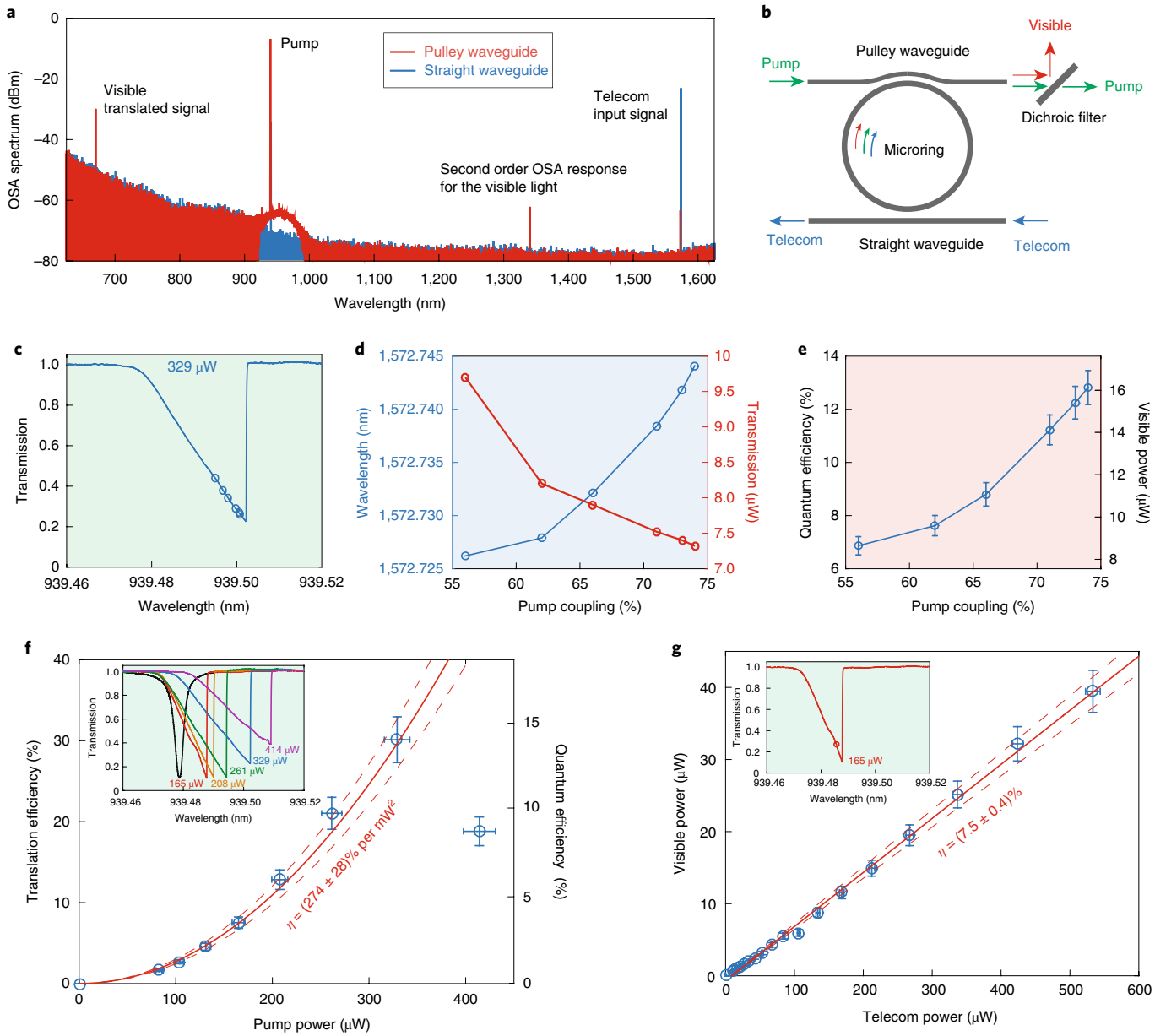

Fig. 4 | Telecom-to-visible nanophotonic spectral translation. a, Optical spectra recorded in the pulley (red) and straight (blue) waveguides for the spectral translation device. The telecom light at 1,572.7 nm (blue) is transferred to a visible wavelength at 669.8 nm (red) through a pump at 939.5 nm, with no other translation channels or noise contribution observed. 0 dB is referenced to 1 mW (that is, dBm). OSA, optical spectrum analyser. **b**, A dichroic filter is used to reject the pump light (>80 dB) to calibrate the visible power accurately in pump-power-dependent measurements. **c**–**e**, Resonance detuning for the pump laser (**c**) and, subsequently, the telecom laser (**d**), to optimize the translation efficiency (**e**). Data are measured with a pump power of (329 ± 13) μW and a telecom power of (53 ± 1) μW. Pump coupling (*x* axes in **d** and **e**) is defined as the percentage of the pump power coupled from the waveguide to the microring, that is, 1 − *T*, where *T* is transmission (*y* axis in **c**). **f**, Translation efficiency (η, left *y* axis) and quantum efficiency (η_Q, right *y* axis) versus pump power. A translation efficiency of $\eta = (30.1 \pm 2.8)\%$ is achieved for (329 ± 13) μW pump power. The quadratic dependence on pump power is a signature of the dFWM process. Solid and dashed red lines represent the quadratic fitting and its one standard deviation confidence range. Inset: corresponding pump transmission traces. Pump detuning is brought close to the bottom of the transmission dip to maximize the translation efficiency. **g**, Output visible power as a function of input telecom power for a fixed pump power of 165 ± 7 μW, with a translation efficiency determined by a linear fit of $\eta = (7.5 \pm 0.4)\%$. The pump detuning is kept constant as indicated by the open circle in the inset transmission trace. Solid and dashed red lines represent the linear fitting and its one standard deviation confidence range. Error bars in **e**–**g** are one standard deviation uncertainties originating from calibration of the on-chip power.

has the smallest footprint among the nanophotonic devices with on-chip integrated waveguides and is 50–1,600 times smaller than the millimetre- and centimetre-scale devices. The spectral translation range is >250 THz and more than an octave, and could be further increased or shifted to other useful spectral bands by simply changing the pump modes (Fig. 2b) and/or reducing the device height and ring width. The typical operating power is sub-milliwatt, which is on par or lower than most other high-*Q* nanophotonic devices, particularly in light of our high translation efficiency of 30%. Although ref. [13] achieves a higher translation efficiency, it uses over 100 times more pump power. To compare with other results in terms of translation efficiency, we consider the measured (or expected) efficiency

Table 1 | Comparison with related state-of-the-art spectral translation devices

Label	Reference	Material	Geometry	Nonlinear process	Dimensions (μm)	$\lambda_s-\lambda_t$ (nm)	P (mW)	$\eta(P)$ (%)	$\eta(P=1\,\mathrm{mW})$ (%)
red ●	This work	Si_3N_4	Microring	$\chi^{(3)}$, dFWM	25/1.15/0.5	1,570–670	0.329	30.1	274
blue ⊗	19	AlN	Microring	$\chi^{(2)}$, SFG	30/1.12/1	1,538–774	9.8	25[a]	2.6[c]
	20	AlN	Microring	$\chi^{(2)}$, SHG	30/1.12/1	1,544–772	27	12	2.5
blue ◇	10	$LiNbO_3$	Microring	$\chi^{(2)}$, SHG	50/0.69/0.55	1,550–775	0.44	0.66	1.5
	21	AlN	Microring	$\chi^{(2)}$, SHG	30/1.2/1	1,560–780	0.96	1.2	1.3[a]/17[b]
red ○	13	Si_3N_4	Microring	$\chi^{(3)}$, FWM-BS	40/1.4/0.48	1,530–960	50/8	96[a]	0.24[a]
	38	$LiNbO_3$	Microdisk	$\chi^{(2)}$, SHG	51/0.7	1,540–770	10	1.1	0.11
blue △	23	GaAs	Microring	$\chi^{(2)}$, SHG	100/1.3/0.15	2,000–1,000	5	0.2	0.04[a]/65[b]
blue ◁	25	GaP	Microdisk	$\chi^{(2)}$, SHG	3.3/0.25	1,545–772	0.35	1.54×10^{-4}[a]	4.4×10^{-4}
blue ▷	39	Si_3N_4	Microring	$\chi^{(2)}$, SHG	116/1.5/0.725	1,554–777	64	0.013	2.0×10^{-4}[a]
red ◇	40	AlN/Si_3N_4	Microring	$\chi^{(3)}$, THG	30/1.2/1	1,560–780	30	0.16	1.8×10^{-4}
blue ▽	26	AlGaAs	Microdisk	$\chi^{(2)}$, SHG	1.9/0.155	1,584–792	1.0	7.0×10^{-5}	7.0×10^{-5}
blue □	18	SiO_2	Microsphere	$\chi^{(2)}$, SHG	62	1,550–775	0.88[c]	4.3×10^{-5}[a]	4.9×10^{-5}
blue ●	8	$LiNbO_3$	mm-resonator	$\chi^{(2)}$, SHG	1,900/500	1,064–532	0.03	9	300
blue ○	7	PPLN	mm-resonator	$\chi^{(2)}$, SHG	1,500/500	1,550–775	9	22	2.4[a]
blue ×	9	PPLN	Waveguide	$\chi^{(2)}$, SHG	4,000/1.4/0.6	1,500–775	20	8	0.4[a,c]
blue ✻	24	GaAs	Waveguide	$\chi^{(2)}$, SHG	1,400	2,000–1,000	2	0.5[a]	0.25[a,c]
red ✻	11	Si	Waveguide	$\chi^{(3)}$, dFWM	20,000	3,550–1,590	300	16,000	0.18[a]
blue +	16	Si_3N_4	Waveguide	$\chi^{(2)}$, SFG	40,000/1.5/0.87	1,547–773	91	0.031	3.3×10^{-4}[a]
red ×	12	Si_3N_4	Waveguide	$\chi^{(3)}$, FWM-BS	18,000/1.2/0.55	1,500–980	11	1.2×10^{-5}	9.9×10^{-8}[a]
red +	16	Si_3N_4	Waveguide	$\chi^{(3)}$, dFWM	40,000/1.5/0.87	1,547–1,540	90	7.9×10^{-4}	9.8×10^{-8}[a]

The table compares the present device with other state-of-the-art devices in terms of material, device geometry, $\chi^{(2)}$ or $\chi^{(3)}$ nonlinear process, dimensions, representative operating wavelengths, pump power and efficiency. The table is organized into two sections, summarizing results from nanophotonic spectral translation devices (top) and millimetre- and centimetre-scale photonic devices (bottom). Dimensions are specified as radius/width/height for microrings, radius/height for microdisks and millimetre resonators, radius for microspheres, and length/width/height for waveguides. λ_s, signal wavelength; λ_t, translated wavelength; η_t, translation efficiency; dFWM, degenerate four-wave mixing; SHG, second-harmonic generation; SFG, sum-frequency generation; FWM-BS, four-wave mixing Bragg scattering. PPLN: periodically poled lithium niobate with poling periods of 14 μm and 4 μm in refs. [79]. [a]Values calculated from representative data. [b]Internal efficiency. [c]Efficiency normalized by waveguide lengths is 2.6% $mW^{-1}cm^{-2}$ and 13% $mW^{-1}cm^{-2}$ in refs. [9,24]. Symbols used in the table correspond to data plotted in Fig. 5.

at 1 mW pump power. Our device has a high efficiency among existing nanophotonic devices of (274 ± 28)% at 1 mW, at least one order of magnitude. This normalized efficiency is also larger than that of most millimetre- and centimetre-scale devices, and is very similar to the highest value in a $\chi^{(2)}$ resonator[8].

Figure 5 provides more detail in comparing the translation efficiency of our work to related studies. $\chi^{(3)}$ works (red symbols) have quadratic power dependence (solid/dashed red lines) and $\chi^{(2)}$ works (blue symbols) have linear power dependence (solid/dashed blue lines). For $\chi^{(2)}$ processes, we have considered both SHG and SFG. We note that although the SHG output signal has a quadratic dependence on pump power, the power scaling for translation efficiency is still linear (because the pump also serves as the input signal). Similarly, for non-degenerate FWM, the power scaling for translation efficiency is the same as degenerate FWM (see Supplementary Information for details). The solid/dashed lines highlight resonator/waveguide performance for $LiNbO_3$ (blue) and Si_3N_4 (red), respectively. The trends are similar to theoretical estimates (Fig. 1d). In the waveguide case, the $\chi^{(2)}$ process is much more efficient than the $\chi^{(3)}$ process (approximately 55 dB difference at 10 mW pump power), because of the much larger nonlinear optical coefficient. However, in the resonator case[8], the two processes are actually expected to be comparable to each other at 1 mW pump power. At 10 mW, our $\chi^{(3)}$ device is projected to be approximately 10 times more efficient than that projected for the $LiNbO_3$ millimetre resonator, provided that the aforementioned close-to-pump FWM could be suppressed. Our work provides a clear demonstration of how a $\chi^{(3)}$ nanophotonic spectral translation device can be comparable to, or even better than, the record $\chi^{(2)}$ device in terms of translation efficiency. We use 1 mW instead of 1 W (the commonly specified power level for SHG) for the comparison point as this is a reasonable operation power for high-Q photonic devices. A comparison at 1 W would be additionally 30 dB more advantageous for the $\chi^{(3)}$ process (Fig. 5).

We want to emphasize that the point of the above comparison is to reveal the importance of optimizing several technical aspects altogether, not just effective nonlinearity and optical quality factor, but also accurate nanophotonic mode engineering targeting specific interacting modes. Although our results are demonstrated on a $\chi^{(3)}$ platform, we believe our methods are equally useful for $\chi^{(2)}$ platforms and may help stimulate significant enhancements in their efficiencies in the future.

Recently, Ramelow and others[14] have discussed how one can view dFWM as an effective $\chi^{(2)}$ process. In our case, one considers the degenerate input (the pump) as being converted to the visible, with the other input (the telecom input in our case) as the pump. The power scaling of such a process is similar to SHG, and single-photon-level nonlinear interactions are in principle possible if the resonant enhancement is sufficiently strong. In ref. [14], the efficiency of conversion from a 350 μW signal at 1,410 nm (the degenerate input) to 1,260 nm is 5%, using an 85 mW pump at 1,590 nm. To evaluate our work in a similar way, we treat the 1,573 nm signal as the effective pump, the 940 nm light (the degenerate input) as the seed and the 670 nm light as the converted output. Our efficiency (Fig. 4d) is (24 ± 2)% at (165 ± 7) μW seed power, with an effective pump power of (533 ± 11) μW. In comparison to ref. [14], this corresponds to a higher efficiency (approximately 5×), a smaller pump power (approximately 200× smaller) and a wider translation range (approximately 5×, or approximately 100 THz larger).

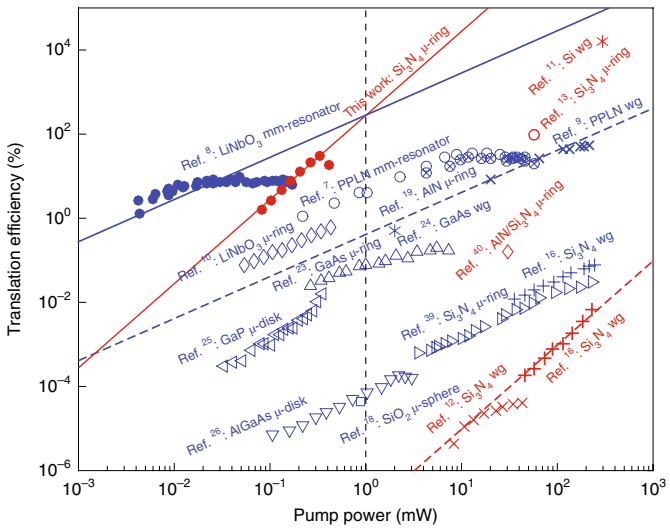

Fig. 5 | Comparison of our nanophotonic spectral translation efficiency with state-of-the-art results. We compare our results with other state-of-the-art devices in terms of translation efficiency versus pump power. Solid/dashed lines show the scaling in $\chi^{(2)}$ $LiNbO_3$ (blue) and $\chi^{(3)}$ Si_3N_4 (red) resonators/waveguides, respectively, which agree with theoretical estimates in that $\chi^{(2)}$ and $\chi^{(3)}$ processes have linear and quadratic power scaling, respectively (ref. [25] is distinguished from others due to its cavity frequency mismatch). Through resonance enhancement and careful mode engineering, our $\chi^{(3)}$ device is projected to reach a translation efficiency of $(274 \pm 28)\%$ at 1 mW, which is comparable to that of the best $\chi^{(2)}$ device. This represents a many order of magnitude improvement relative to the waveguide case, where the $\chi^{(3)}$ process is over 50 dB smaller in efficiency than the $\chi^{(2)}$ case at 10 mW. μ, micro; wg, waveguide.

Discussion

In summary, by using SFMF engineering and precise mode identification to enable phase- and frequency-matched operation, we have demonstrated high-efficiency spectral translation from telecom to visible wavelengths using dFWM in a Si_3N_4 nanophotonic resonator. We propose and demonstrate that a $\chi^{(3)}$ device can be comparable to, or even superior than, state-of-the-art $\chi^{(2)}$ devices for wide-band spectral translation. The demonstrated translation efficiency at sub-milliwatt pump power improves the current record in nanophotonic devices by at least one order of magnitude. This approach holds great promise for many applications, such as connecting visible-wavelength atomic references to the telecommunications band.

Online content

Any methods, additional references, Nature Research reporting summaries, source data, statements of code and data availability and associated accession codes are available at https://doi.org/10.1038/s41566-019-0464-9.

Received: 22 February 2019; Accepted: 3 May 2019;
Published online: 24 June 2019

References

1. Boyd, R. W. *Nonlinear Optics* (Academic Press, 2008).
2. Agrawal, G. *Nonlinear Fiber Optics* (Academic Press, 2007).
3. Komljenovic, T. et al. Heterogeneous silicon photonic integrated circuits. *J. Lightwave Technol.* **34**, 20–35 (2016).
4. Spencer, D. T. et al. An optical-frequency synthesizer using integrated photonics. *Nature* **557**, 81–85 (2018).
5. Ludlow, A. D., Boyd, M. M., Ye, J., Peik, E. & Schmidt, P. O. Optical atomic clocks. *Rev. Mod. Phys.* **87**, 637–701 (2015).
6. Riehle, F. Optical clock networks. *Nat. Photon.* **11**, 25–31 (2017).
7. Ilchenko, V. S., Savchenkov, A. A., Matsko, A. B. & Maleki, L. Nonlinear optics and crystalline whispering gallery mode cavities. *Phys. Rev. Lett.* **92**, 043903 (2004).
8. Fürst, J. U. et al. Naturally phase-matched second-harmonic generation in a whispering-gallery-mode resonator. *Phys. Rev. Lett.* **104**, 153901 (2010).
9. Wang, C. et al. Ultrahigh-efficiency wavelength conversion in nanophotonic periodically poled lithium niobate waveguides. *Optica* **5**, 1438–1441 (2018).
10. Luo, R. et al. Optical parametric generation in a lithium niobate microring with modal phase matching. *Phys. Rev. Appl.* **11**, 034026 (2019).
11. Liu, X. et al. Bridging the mid-infrared-to-telecom gap with silicon nanophotonic spectral translation. *Nat. Photon.* **6**, 667–671 (2012).
12. Agha, I., Ates, S., Davanco, M. & Srinivasan, K. A chip-scale, telecommunications-band frequency conversion interface for quantum emitters. *Opt. Express* **21**, 1476–1478 (2013).
13. Li, Q., Davanço, M. & Srinivasan, K. Efficient and low-noise single-photon-level frequency conversion interfaces using silicon nanophotonics. *Nat. Photon.* **10**, 406–414 (2016).
14. Ramelow, S. et al. Strong nonlinear coupling in a Si_3N_4 ring resonator. *Phys. Rev. Lett.* **122**, 153906 (2019).
15. Hickstein, D. D. et al. Self-organized nonlinear gratings for ultrafast nanophotonics. Preprint at *arXiv* https://arxiv.org/abs/1806.07547 (2018).
16. Grassani, D., Pfeiffer, M. H. P., Kippenberg, T. J. & Brès, C.-S. Second- and third-order nonlinear wavelength conversion in an all-optically poled Si_3N_4 waveguide. *Opt. Lett.* **44**, 106–109 (2019).
17. Ferrera, M. et al. Low-power continuous-wave nonlinear optics in doped silica glass integrated waveguide structures. *Nat. Photon.* **2**, 737–740 (2008).
18. Zhang, X. et al. Symmetry-breaking-induced nonlinear optics at a microcavity surface. *Nat. Photon.* **13**, 21–24 (2019).
19. Guo, X., Zou, C. L., Jung, H. & Tang, H. X. On-chip strong coupling and efficient frequency conversion between telecom and visible optical modes. *Phys. Rev. Lett.* **117**, 123902 (2016).
20. Guo, X., Zou, C.-L. & Tang, H. X. Second-harmonic generation in aluminum nitride microrings with 2,500%/W conversion efficiency. *Optica* **3**, 1126–1131 (2016).
21. Bruch, A. W. et al. 17,000%/W second-harmonic conversion efficiency in single-crystalline aluminum nitride microresonators. *Appl. Phys. Lett.* **113**, 131102 (2018).
22. Chang, L. et al. Thin film wavelength converters for photonic integrated circuits. *Optica* **3**, 531–535 (2016).
23. Chang, L. et al. High efficiency SHG in heterogenous integrated GaAs ring resonators. *APL Photon.* **4**, 036103 (2019).
24. Chang, L. et al. Heterogeneously integrated GaAs waveguides on insulator for efficient frequency conversion. *Laser Photon. Rev.* **12**, 1800149 (2018).
25. Lake, D. P. et al. Efficient telecom to visible wavelength conversion in doubly resonant gallium phosphide microdisks. *Appl. Phys. Lett.* **108**, 031109 (2016).
26. Mariani, S. et al. Second-harmonic generation in AlGaAs microdisks in the telecom range. *Opt. Lett.* **39**, 3062–3065 (2014).
27. Lu, X. et al. Chip-integrated visible-telecom photon pair sources for quantum communication. *Nat. Phys.* **15**, 373–381 (2019).
28. Okawachi, Y. et al. Octave-spanning frequency comb generation in a silicon nitride chip. *Opt. Lett.* **36**, 3398–3400 (2011).
29. Li, Q. et al. Stably accessing octave-spanning microresonator frequency combs in the soliton regime. *Optica* **4**, 193–203 (2017).
30. Karpov, M., Pfeiffer, M. H., Liu, J., Lukashchuk, A. & Kippenberg, T. J. Photonic chip-based soliton frequency combs covering the biological imaging window. *Nat. Commun.* **9**, 1146 (2018).
31. Kippenberg, T. J., Spillane, S. M. & Vahala, K. J. Kerr-nonlinearity optical parametric oscillation in an ultrahigh-*Q* toroid microcavity. *Phys. Rev. Lett.* **93**, 083904 (2004).
32. Yariv, A. & Yeh, P. *Photonics: Optical Electronics in Modern Communications* (Oxford Univ. Press, 2006).
33. Caspani, L. et al. Integrated sources of photon quantum states based on nonlinear optics. *Light Sci. Appl.* **6**, e17100 (2017).
34. Shah Hosseini, E., Yegnanarayanan, S., Atabaki, A. H., Soltani, M. & Adibi, A. Systematic design and fabrication of high-*Q* single-mode pulley-coupled planar silicon nitride microdisk resonators at visible wavelengths. *Opt. Express* **18**, 2127–2136 (2010).
35. Lu, X., Rogers, S., Jiang, W. C. & Lin, Q. Selective engineering of cavity resonance for frequency matching in optical parametric processes. *Appl. Phys. Lett.* **105**, 151104 (2014).
36. Helt, L. G., Liscidini, M. & Sipe, J. E. How does it scale? Comparing quantum and classical nonlinear optical processes in integrated devices. *J. Opt. Soc. Am. B* **29**, 2199–2212 (2012).
37. Hummon, M. T. et al. Photonic chip for laser stabilization to an atomic vapor with 10^{-11} instability. *Optica* **5**, 443–449 (2018).
38. Lin, J. et al. Phase-matched second-harmonic generation in an on-chip $LiNbO_3$ microresonator. *Phys. Rev. Appl.* **6**, 014002 (2016).

39. Levy, J. S., Foster, M. A., Gaeta, A. L. & Lipson, M. Harmonic generation in silicon nitride ring resonators. *Opt. Express* **19**, 11415–11421 (2011).
40. Surya, J. B., Guo, X., Zou, C.-L. & Tang, H. X. Efficient third harmonic generation in composite aluminum nitride/silicon nitride microrings. *Optica* **5**, 103–108 (2017).

Acknowledgements

This work is supported by the DARPA DODOS and NIST-on-a-chip programmes. X.L., G.M., Q.L. and A.S. acknowledge support under the Cooperative Research Agreement between the University of Maryland and NIST-PML (award no. 70NANB10H193).

Author contributions

X.L. led the design, fabrication and measurement of the spectral translation devices. G.M., A.S., Q.L. and K.S. provided assistance with design and measurements. D.A.W. and Q.L. provided assistance with fabrication. All authors participated in analysis and discussion of results. X.L. and K.S. wrote the manuscript with assistance from all authors and K.S. supervised the project.

Competing interests

The authors declare no competing interests.

Additional information

Supplementary information is available for this paper at https://doi.org/10.1038/s41566-019-0464-9.

Reprints and permissions information is available at www.nature.com/reprints.

Correspondence and requests for materials should be addressed to X.L. or K.S.

Publisher's note: Springer Nature remains neutral with regard to jurisdictional claims in published maps and institutional affiliations.

Methods

Device fabrication. The device layout was achieved with the Nanolithography Toolbox, a free software package developed by the NIST Center for Nanoscale Science and Technology[41]. The 500-nm-thick Si_3N_4 layer was deposited by low-pressure chemical vapour deposition on top of a 3-μm-thick thermal SiO_2 layer on a 100-mm-diameter Si wafer. The wavelength-dependent refractive index and thickness of the layers were measured using a spectroscopic ellipsometer, with the data fit to an extended Sellmeier model. The device pattern was created in positive-tone resist by electron-beam lithography. The pattern was then transferred to Si_3N_4 by reactive-ion etching using CF_4/CHF_3 chemistry. The device was chemically cleaned to remove deposited polymer and remnant resist, and then annealed at 1,100 °C in an N_2 environment for 4 h. An oxide liftoff process was performed so that the microrings had an air cladding on top while the input/output edge-coupler waveguides had SiO_2 on top to form more symmetric modes for coupling to optical fibres. The facets of the chip were polished for lensed-fibre coupling. After polishing, the chip was annealed again at 1,100 °C in an N_2 environment for 4 h.

Translation efficiency. Throughout this Article, we assessed the efficiency of spectral translation based on optical power. The translation efficiency η is defined as P_{SHG}/P_{pump} for SHG ($\chi^{(2)}$) and as $P_{translated}/P_{signal}$ for other nonlinear processes, that is, SFG/DFG ($\chi^{(2)}$) and dFWM and FWM-BS ($\chi^{(3)}$). Here, P represents the optical power on-chip and in the waveguide unless specified otherwise (see Supplementary Information for the itemized losses in the testing set-up). The other figure of merit is quantum efficiency (η_Q), which is defined as N_{SHG}/N_{pump} and $N_{translated}/N_{signal}$ for SHG and other processes, where N represents photon flux on-chip and in the waveguide. In our work, the ratio of the translation efficiency and photon flux efficiency is 2.35, which equals the ratio of the photon energies at 669.8 nm and 1,572.7 nm.

We note that the definition of translation efficiency is mathematically equivalent to that of conversion efficiency, which is commonly adopted in the field. However, from a quantum-mechanical point of view, telecom photons are not annihilated to generate visible photons in the described FWM process. Instead, two pump photons are annihilated to generate telecom and visible photons. We therefore adopt the terminology of spectral translation from previous FWM works[11], which is more appropriate than conversion efficiency in our case.

Data availability

The data that supports the plots within this paper and other findings of this study are available from the corresponding author upon reasonable request.

References

41. Balram, K. C. et al. The nanolithography toolbox. *J. Res. NIST* **121**, 464–475 (2016).